Comput Mech (2009) 44:447–453
DOI 10.1007/s00466-009-0384-5

ORIGINAL PAPER

An immersed boundary method to solve fluid–solid interaction problems

Dedy Zulhidayat Noor · Ming-Jyh Chern · Tzyy-Leng Horng

Received: 5 June 2008 / Accepted: 2 March 2009 / Published online: 24 March 2009

Abstract We describe an immersed-boundary technique which is adopted from the direct-forcing method. A virtual force based on the rate of momentum changes of a solid body is added to the Navier–Stokes equations. The projection method is used to solve the Navier–Stokes equations. The second-order Adam–Bashford scheme is used for the temporal discretization while the diffusive and the convective terms are discretized using the second-order central difference and upwind schemes, respectively. Some benchmark problems for both stationary and moving solid object have been simulated to demonstrate the capability of the current method in handling fluid–solid interactions.

Keywords Immersed-boundary · Direct-forcing · Virtual force · Projection method

1 Introduction

Interactions between fluids and structures are frequently encountered in nature. In many engineering applications, in terms of computational fluid dynamics, these problems require modeling of complex geometries. The common method to simulate the flow with a complex boundary is the body-fitted or unstructured grid methods. However, these method need high computational cost and memory requirements, especially in the case of a moving body due to transient re-meshing strategies at each time step.

In particular, the immersed boundary method has been getting popular in the last few years since it was introduced by Peskin [14] due to its ability to handle simulations for a moving complex boundary with less computational cost and memory requirements than the body-fitted method. The numerical implementation of an immersed boundary method employs a fixed Cartesian grid for a fluid and a Lagrangian grid for an immersed boundary. The immersed boundary is modeled by a singular force which is incorporated into the forcing terms, **f**, in the Navier–Stokes equations. The interaction between the fluid and the immersed boundary is linked through the spreading of the singular force from the Lagrangian grid to the Cartesian grid and the interpolation of the velocity from the Cartesian grid to the Lagrangian grid using a discrete Dirac delta function. Furthermore, some modifications and improvements of this method have been proposed by some other manuscripts [7,8,11,16,17]. These methods can be categorized as continuous forcing method wherein a forcing term is added to the continuous Navier–Stokes equations before they are discretized.

Instead of using a delta function to distribute force from a Lagrangian grid to a Cartesian grid, Yusof [23] introduced a new immersed boundary method, namely the direct-forcing method. This method uses a forcing term determined by the difference between the interpolated velocities on the boundary points and the desired boundary velocities. This method is also known as the discrite forcing method since the forcing is either explicitly or implicitly applied to the discretized Navier–Stokes equations. The idea of the direct-forcing method has been used and developed successfully in some applications [6,19,20,24,25].

Electronic supplementary material The online version of this article (doi:10.1007/s00466-009-0384-5) contains supplementary material, which is available to authorized users.

D. Z. Noor (✉) · M.-J. Chern
Department of Mechanical Engineering, National Taiwan University of Science and Technology, Taipei 10607, Taiwan
e-mail: D9503802@mail.ntust.edu.tw; zulnoor@me.its.ac.id

T.-L. Horng
Department of Applied Mathematics, Feng Chia University, Taichung 40742, Taiwan

One of the successful applications of the direct-forcing idea is the method introduced by Fadlun et al. [6]. They developed combined immersed boundary finite difference methods for three dimensional complex flow simulations. Some cases including the flow inside an IC piston/cylinder assembly at high Reynolds number were simulated successfully. The major issue of their work is the interpolation of the forcing over the grid that determines the accuracy of the scheme. They implemented three different procedures, i.e., no interpolation or stepwise geometry, volume fraction weighting and velocity interpolation. They calculated the effect of those procedures on the accuracy of the scheme and found that the last procedure which has a second order accuracy gave the best results.

In this present work, we propose an immersed boundary method to simulate fluid–solid interaction by adopting the direct-forcing method. A virtual force term is added to the incompressible Navier–Stokes equations in order to accommodate interaction between solids and fluids. The body is identified by a volume-of-body function, η. The body interior is viewed as being occupied by the same incompressible fluids as outside with a prescribed velocity field. Since the body velocity is assumed to be incompressible, the pressure field inside the body obeys the same governing equation as the pressure outside. η denotes a fraction of solids within a cell where η equal to 1 and 0 for solid and fluid cells, respectively, and be fractional on boundary cells. In the case of a moving object, for making the scheme straightforward and robust, we ignore the fractional value of η. The values of η is either 1 or 0 only. As an example, for the case of a circular cylinder, we defined η by following the function

$$\eta(x, y, t) = \begin{cases} 1, & (x - x_c(t))^2 + (y - y_c(t))^2 \leq R^2 \\ 0, & (x - x_c(t))^2 + (y - y_c(t))^2 > R^2 \end{cases} \quad (1)$$

where $x_c(t)$ and $y_c(t)$ are the x and y coordinates of the center of the cylinder at particular time t, respectively, and R is the radius of the cylinder. Furthermore, the cells number 1 and 3 in Fig. 1 belong to fluids ($\eta = 0$), on the other hand, the cells number 2 and 4 belong to solid ($\eta = 1$). It is the reason that we chose the volume of solid (VOS) method instead of using a velocity interpolation method even thought the later as reported by Fadlun et al. [6] is better in accuracy. The accuracy of the present method can be enhanced by implementing a fine grid arrangement near by the solid–fluid boundary [10]. Details of the numerical procedure are presented in the following section. Finally we simulated problems including moving body cases to demonstrate the capability of the present method in handling fluid–solid interactions.

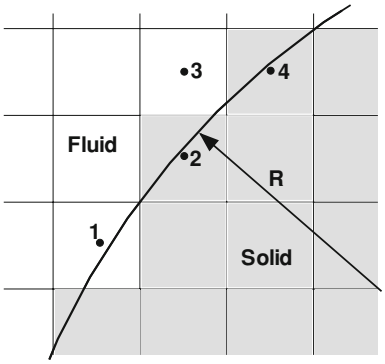

Fig. 1 Computational cells around solid–fluid boundary

2 Numerical method

The non-dimensional governing equations for an unsteady incompressible fluid flow can be written as follows,

$$\frac{\partial \mathbf{u}}{\partial t} + \nabla \cdot (\mathbf{uu}) = -\nabla p + \frac{1}{Re}\nabla^2 \mathbf{u} + \mathbf{f} \quad (2)$$

$$\nabla \cdot \mathbf{u} = 0, \quad (3)$$

where $\mathbf{u}$ is the velocity vector, p is the pressure, $\mathbf{f}$ is the virtual force term and Re is the Reynolds number.

2.1 Numerical procedure

We use a three-step time-split scheme to advance the flow field. First the velocity is stepped from the nth time level to the first intermediate level "*" by solving the advection-diffusion equations without the pressure and virtual force for the momentum Eq. 2. Subsequently, this step can be stated in the following forms

$$\frac{\mathbf{u}^* - \mathbf{u}^n}{\Delta t} = S^n, \quad (4)$$

where S is the convective and diffusive terms of the momentum equations. We use the second-order Adam–Bashford method for the temporal discretization in such a way that term S can be rewritten as

$$S^n = \frac{3}{2}\left(-\nabla \cdot (\mathbf{uu}) + \frac{1}{Re}\nabla^2 \mathbf{u}\right)^n - \frac{1}{2}\left(-\nabla \cdot (\mathbf{uu}) + \frac{1}{Re}\nabla^2 \mathbf{u}\right)^{n-1}. \quad (5)$$

The convective and diffusive terms of the momentum equations are discretized using the second-order upwind and the central difference scheme, respectively, which are briefly given below.

At the x-direction, for example, the convective terms are $u\partial u/\partial x + v\partial u/\partial y$. Therefore, the discretization becomes

$$u\frac{\partial u}{\partial x} = \frac{1}{2\Delta x}\left(u^{+}\left(3u_{i,j} - 4u_{i-1,j} + u_{i-2,j}\right) + u^{-}\left(-u_{i+2,j} + 4u_{i+1,j} - 3u_{i,j}\right)\right) \tag{6}$$

where $u^{+} = 0.5(u_{i,j} + |u_{i,j}|)$ and $u^{+} = 0.5(u_{i,j} - |u_{i,j}|)$. Similarly for other components and directions.

On the other hand, the diffusive term is discretized by the second-order central difference scheme, for the x-direction,

$$\frac{\partial^2 u}{\partial x^2} = \frac{u_{i+1,j} - 2u_{i,j} + u_{i-1,j}}{\Delta x^2} \quad \text{and} \quad \frac{\partial^2 u}{\partial y^2} = \frac{u_{i,j+1} - 2u_{i,j} + u_{i,j-1}}{\Delta y^2}. \tag{7}$$

Similarly for the other directions.

The intermediate velocity in Eq. 4, in general, does not satisfy the divergence-free condition in Eq. 3. At the second step we march the first intermediate velocity by including the pressure term

$$\frac{\mathbf{u}^{**} - \mathbf{u}^{*}}{\Delta t} = -\nabla p^{n+1}. \tag{8}$$

Applying the divergence on both sides of Eq. 8 becomes

$$\frac{\nabla\cdot\mathbf{u}^{**} - \nabla\cdot\mathbf{u}^{*}}{\Delta t} = -\nabla^2 p^{n+1}. \tag{9}$$

Due to conservation of mass we have

$$\nabla\cdot\mathbf{u}^{**} = 0. \tag{10}$$

Then substitution of Eq. 10 to Eq. 9 gives the Poisson equation

$$\nabla^2 p^{n+1} = \frac{1}{\Delta t}\nabla\cdot\mathbf{u}^{*}. \tag{11}$$

Once Eq. 11 is solved, we can advance the intermediate velocity in Eq. 8. Furthermore, we update the velocity to the $(n+1)$th time level by imposing the force term as follow

$$\frac{\mathbf{u}^{n+1} - \mathbf{u}^{**}}{\Delta t} = \mathbf{f}^{n+1}. \tag{12}$$

The terms $\mathbf{u}^{*}$ and $\mathbf{u}^{**}$ are the first and the second intermediate velocity, respectively. The pressure term in Eq. 9 is determined by solving the Poisson problem in Eq. 11 that arises from applying the discrete divergence operator and using the fact that we want to satisfy the condition in Eq. 3.

2.2 The virtual force treatment

The virtual force term, $\mathbf{f}$, in Eq. 2 represents the action of a solid upon a fluid. This force reveals the existence of resultant force to hold or drive a solid body when it is stationary or moving. To satisfy the no-slip boundary condition for solid motion, the force acting on the solid should ensure that the fluid velocity ($\mathbf{u}$) equal to the solid velocity ($\mathbf{u}_s$) at the $(n+1)$th time step, i.e., $\mathbf{u}^{n+1} = \mathbf{u}_s^{n+1}$. Thence, the virtual force is defined as the rate of momentum changes of solid body and proportional the difference between the solid velocity at the $(n+1)$th time step and the fluid velocity at the nth time step. This force exists on the solid body and zero elsewhere. Furthermore, it can be simply written as

$$\mathbf{f}^{n+1} = \eta\frac{\mathbf{u}^{n+1} - \mathbf{u}^{n}}{\Delta t} = \eta\frac{\mathbf{u}_s^{n+1} - \mathbf{u}^{n}}{\Delta t}, \tag{13}$$

where $\mathbf{u}_s$ is the prescribed velocity of a solid body. We use a staggered grid arrangement, i.e., the pressure is located at the center of the cell while the velocities are placed at the faces of the cell. Note that $\mathbf{u}$ in Eq. 13 is the velocity at the center of the cell which is interpolated from its faces.

The scheme is simple since there is no special treatment to couple the solid–fluid interface. At any particular time, any location/cell within computational domain which has $\eta = 1$ is judged as a solid cell and it is considered as the same incompressible fluid as outside with a prescribed velocity as mentioned before. The pressure field inside the body (solid) is treated as same as the pressure field outside (fluid). The different between moving body cases and stationary body cases in the proposed method is the definition of $\mathbf{u}_s$ in Eq. 13. $\mathbf{u}_s(x, y, t)$ is given for moving object cases and it is vanished for the stationary ones. Therefore, for the same grid size, there is no different computational time between stationary and moving body cases due to a fixed grid arrangement. Subsequently it reduces computational cost and memory requirements, especially for moving object cases. Anyway, apart from the simplicity and advantages mentioned above, the application of the present method is limited only for the cases with a prescribed velocity of solids.

Instead of using the integration method over a solid surface, especially for the case of a moving object, it is more convenient and easier to transform it into a volume integral over the body volume in such a way that the forces acting on the immersed body can be calculated as

$$\bar{\mathbf{f}} = \sum_{i=1}^{N}\mathbf{f}_i\Delta\forall_i, \tag{14}$$

where $\Delta\forall_i$ and N are volume of ith cell and total number of cells, respectively.

Finally, a complete numerical procedure for each time step of the proposed method is given below

1. Detect the location of boundary cells and determine $\eta(x, y, t)$.
2. Calculate the first intermediate velocity in Eq. 4.
3. Solve the Poisson equation (Eq. 11) and advance the intermediate velocity (Eq. 8).

4. Calculate the virtual force (Eq. 13). Immediately after we have the calculated force, the drag and lift force acting on the solid can be easily obtained by taking summation of these forces in x- and y-directions (Eq. 14).
5. Update velocity using the calculated virtual force (Eq. 12).
6. Repeat the same procedures (1–5) for the next time step.

3 Numerical results and discussion

3.1 The flow past a stationary circular cylinder

The flow past a stationary circular cylinder immersed in an unbounded uniform flow has been investigated experimentally [3,18,21] and numerically [1,2,4,15,22]. It is a benchmark problem for numerical validation. We consider simulations at Reynolds numbers of $Re = 40$ and $Re = 100$ to validate the present numerical method.

The instantaneous streamline contours for both cases are presented in Figs. 2 and 3. It is well known that at low Re, the flow pattern remains symmetric with stationary recirculating vortices behind the cylinder (Fig. 2). Increasing of Re leads to the instability of flow structures, a pair of symmetrical vortices behind cylinder breaks down and the vortex starts to shed up and down alternatively (Fig. 3). This shedding frequency can be revealed as an dimensionless frequency, namely Strouhal number.

The comparison of the drag coefficient (C_D), the recirculation length (l_w) and the Strouhal number (S_t) with some previous studies is shown in Table 1. Since the proposed model is established for an unsteady flows, it is interesting to check if the present numerical method can correctly predict the complete flow evolution process. The instantaneous wake length, l_w, may be considered an evolution parameter. Figure 4 illustrates the wake evolution at $Re = 40$ obtained using several experimental and numerical models. It is found that our results have a good agreement with those of the previous results.

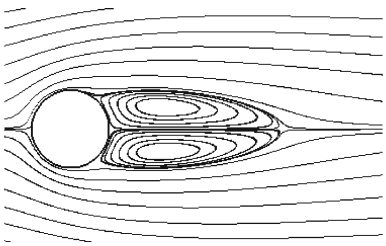

Fig. 2 Instantaneous streamlines, $Re = 40$

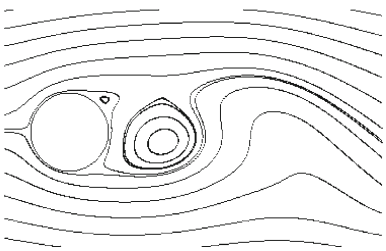

Fig. 3 Instantaneous streamlines, $Re = 100$

Table 1 The comparison of average drag coefficients, recirculation length and Strouhal number at $Re = 40$ and $Re = 100$

Authors	$Re = 40$		$Re = 100$	
	C_D	l_w	C_D	S_t
Borthwick [1]	1.507	–	–	–
Tritton [18]	1.480	–	–	–
Chern et al. [2]	1.480	2.20	–	–
Dennis and Chang [4]	1.522	2.35	–	–
Su et al. [17]	1.630	–	1.40	0.168
Dias and Majumdar [5]	1.540	2.69	1.395	0.171
Pan [13]	1.510	2.18	1.32	0.16
Tseng and Ferziger [19]	1.530	2.21	1.42	0.164
Present study	1.560	2.219	1.4	0.167

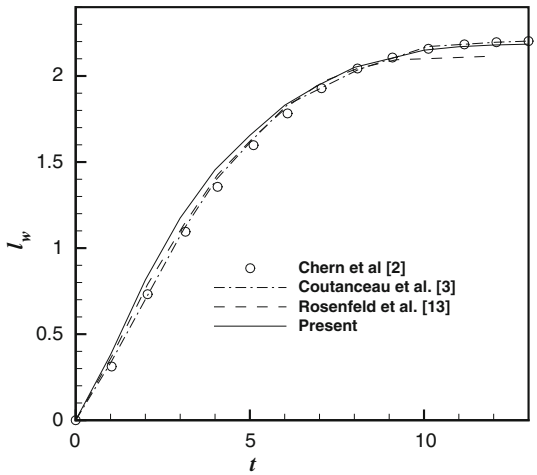

Fig. 4 Wake evolution, $Re = 40$

3.2 The flow past stationary circular cylinders in tandem arrangement

We simulated flow over circular cylinders in a tandem arrangement at $Re = 200$. The center to-center distance (L) equal to $3D$ and $4D$ are chosen to cover the critical spacing and comparable with the previous study [12]. The instantaneous vorticity contours for both cases are showed in Fig. 5 while the drag coefficients (C_D) and Strouhal numbers (S_t) are presented in Table 2.

For the case of $L/D = 3$, the cylinders act as a single body. The separating shear layer from the upstream cylinder covers

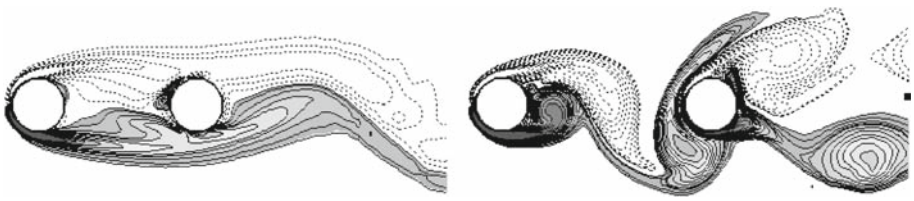

Fig. 5 Instantaneous streamlines and vorticity contours, $Re = 200$, $L/D = 3.0$ $(left)$ and $L/D = 4.0$ $(right)$

Table 2 Average drag coefficients and Strouhal numbers for cylinder in tandem arrangement at $Re = 200$

L/D	Meneghini et al. [12]			Present study		
	C_{D1}	C_{D2}	S_t	C_{D1}	C_{D2}	S_t
3.0	1.0	−0.08	0.125	0.992	−0.11	0.127
4.0	1.18	0.38	0.174	0.119	0.381	0.178

Index 1 refers to the upstream cylinder and index 2 to the downstream cylinder

Table 3 Average drag coefficients and Strouhal numbers for cylinder in side-by-side arrangement at $Re = 200$

L/D	Meneghini et al. [12]		Present study	
	C_{D1}	C_{D2}	C_{D1}	C_{D2}
3.0	1.32	1.32	1.342	1.342
4.0	1.41	1.41	1.421	1.421

Index 1 refers to the upper cylinder and index 2 to the lower cylinder

the downstream cylinder with only one vortex wake forming behind the downstream cylinder. The drag coefficient of the downstream cylinder is lower than the upstream one and has a negative value since it is placed in a low pressure region inside the wake behind the upstream cylinder. As the spacing increases to $L/D = 4$, vortex shedding occurs from both cylinders. The wake behind the downstream cylinder is formed by the combination of vortex shed from the upstream and the downstream cylinder.

Comparing with $L/D = 3$, the drag coefficient of upstream cylinder increases and the drag of the downstream cylinder become positive even though it is lower than the upstream one. The values of C_D and S_t in Table 2 showed that the present simulations have a good agreement with those of the previous study [12].

3.3 The flow past stationary circular cylinders in side-by-side arrangement

We also simulated the flow over circular cylinders in a side-by-side arrangement. The flows at $Re = 200$ with the spacing of 1.5 and 3 are presented to compare with the previous study [12]. The vorticity contours and the drag coefficients are presented in Fig. 6 and Table 3, respectively.

Simulation at a small gap ($L/D = 1.5$), showed that the wake behavior has a similar behavior with a single cylinder. The wake which is deflected towards one of the cylinders increases the drag compare to a single cylinder. In our simulation for $L/D = 3$, the wakes behind each cylinder are asymmetrical and has the drag coefficient larger than the simulation for $L/D = 1.5$. It was noted that for both cases, the drag coefficient of the upper and the lower cylinder are the same and deal with the result of [12] as shown in Table 3.

3.4 The flow past an in-line oscillating cylinder

To further demonstrate the performance of the present method, we undertook simulation for the flow past an in-line oscillating cylinder at Reynolds number 100. The cylinder

Table 4 The comparisons of lift and drag coefficients of in-line oscillating cylinder at $Re = 100$

	Hurlbut et al. [9]		Su et al. [17]		Present study	
f_c/f_s	0	2	0	2	0	2
C_D	1.4	1.7	1.41	1.68	1.413	1.671
$C_{L\max}$	0.34	0.97	0.31	0.95	0.325	0.982

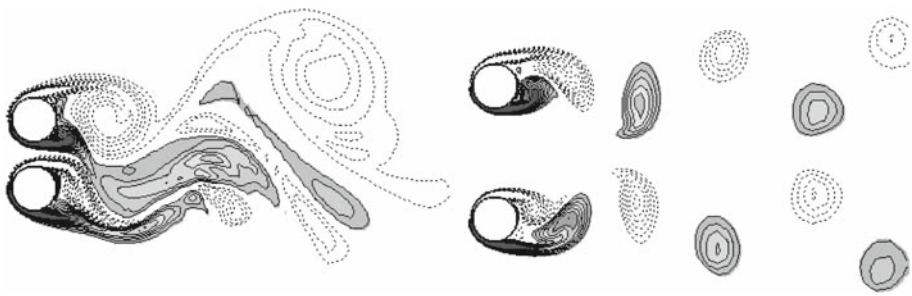

Fig. 6 Instantaneous streamlines and vorticity contours, $Re = 200$, $L/D = 1.5$ $(left)$ and $L/D = 3.0$ $(right)$

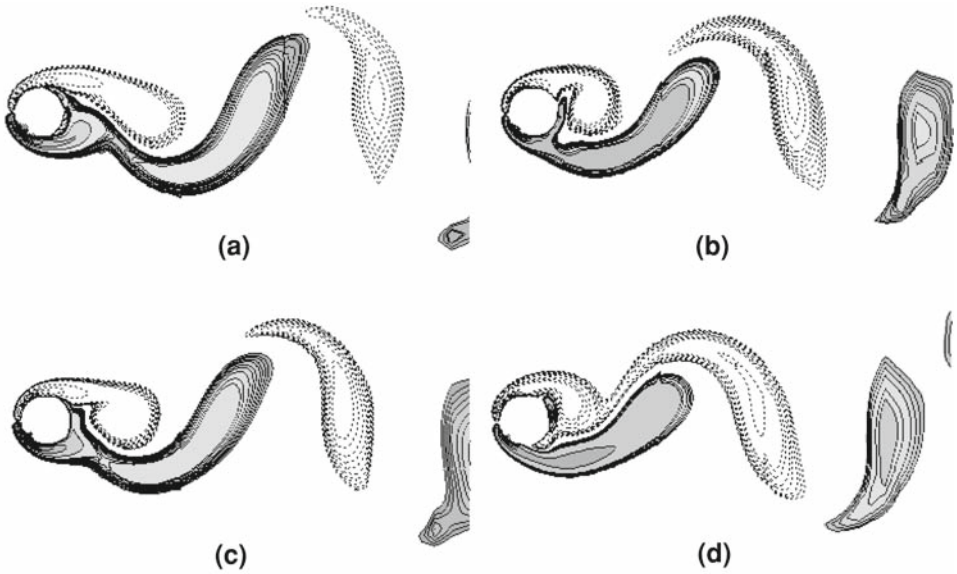

Fig. 7 The instantaneous vorticity contours near the oscillating cylinder at $Re = 100$; *dotted and solid lines* denote negative and positive contours: **a** $t = T/4$, **b** $t = T/2$, **c** $t = 3T/4$, **d** $t = T$ (T is the oscillation period of the cylinder)

is oscillated parallelly to the free stream at a frequency (f_c) equal to two times the vortex shedding frequency (f_s) of the single fixed cylinder ($f_c = 2f_s$). This kind of simulation has been performed numerically by Hurlbut et al. [9] and Su et al. [17]. The cylinder is set to move horizontally following the equation of motion, i.e., $U_{(x)} = 0.14D\cos(2\pi f_c t)$, where the amplitude of the oscillation is 0.14 of the cylinder diameter D. In our simulation, $U_{(x)}$ denotes $\mathbf{u}_s$ in Eq. (13).

It is known that the in-line oscillation of the cylinder at a range near twice the shedding frequency of the stationary cylinder causes the synchronization, subsequently increase both the drag and lift force acting on the cylinder. The comparison of the calculated drag and lift coefficients with the previous study is presented in Table 4 and showed that the synchronization was successfully captured using the proposed method. The instantaneous vorticity contours during a period of cylinder oscillation are showed in Fig. 7.

4 Conclusions

In the present study, we developed an immersed boundary technique using a virtual force method to deal with solid–fluid interaction. The Navier–Stokes equations are solved using the projection method with two intermediate velocities. The second-order Adam–Bashford scheme is used for the temporal discretization while the second-order central difference and upwind scheme are used for the spatial discretization of diffusive and convective terms, respectively. Our simulations for some benchmark problems covering both stationary and moving object have showed that the proposed method has the capability to handle solid–fluid interaction problems. Finally, we found that the proposed method is easy to be implemented in simulations of fluid–solid interactions.

Acknowledgments Funding from the National Taiwan University of Science and Technology (NTUST) is gratefully acknowledged by the authors. The project is also supported by the National Science Council Taiwan under the grant NSC 96-2221-E-001-098-MY3. Authors would like to thank the computing center of NTUST for providing the computing facility in the university cluster.

References

1. Borthwick AGL (1986) Comparison between two finite difference schemes for computing the flow around a cylinder. Int J Numer Methods Fluids 6:275–290
2. Chern MJ, Borthwick AGL, Taylor R (2005) Pseudospectral element model for free surface viscous flows. Int J Numer Methods Heat Fluid Flow 15:517–554
3. Coutanceau M, Bouard R (1977) Experimental determination of the main features of the viscous flow in the wake of a circular cylinder in uniform translation. Part 1. Steady flow. J Fluid Mech 79:231
4. Dennis SCR, Chang GZ (1970) Numerical solutions for steady flow past a circular cylinder at Reynolds numbers up to 100. J Fluid Mech 42:471–489
5. Dias A, Majumdar S, Numerical computation of flow around a circular cylinder, Technical Report, PS II Report, BITS Pilani, India
6. Fadlun EA, Verzicco R, Orlandi P, Yusof JM (2000) Combined immersed-boundary finite-difference methods for three dimensional complex flow simulations. J Comput Phys 161:35–60
7. Goldstein D, Handler R, Sirovich L (1993) Modeling an no-slip flow boundary with an external force field. J Comput Phys 105: 354–366
8. Goldstein D, Handler R, Sirovich L (1995) Direct numerical simulation of turbulent flow over a modelled riblet covered surface. J Comput Phys 302:333
9. Hurlbut SE, Spaulding ML, White FM (1982) Numerical solution for laminar two dimensional flow about a cylinder oscillating in a uniform stream. Trans ASME J Fluids Eng 104:214
10. Kalitzin G, Iaccarino G (2003) Toward immersed boundary simulation of high Reynolds number flows, Annual Research Briefs, Center for Turbulence Research, pp 369–378

11. Lai MC, Peskin CS (2000) An Immersed boundary method with formal second-order accuracy and reduced numerical viscosity. J Comput Phys 160:705–719
12. Meneghini JR, Saltara F, Siqueira CLR, Ferrari JJr (2001) A. Numerical simulation of flow in interference between two circular cylinders in tandem and side-by-side arrangements. J Fluids Struct 15:327–350
13. Pan D (2006) An immersed boundary method on unstructured cartesian meshes for incompressible flow with heat transfer. Numer Heat Transf Part B 49:277–297
14. Peskin CS (1972) Flow patterns around heart valves: a numerical method. J Comput Phys 10:252–271
15. Rosenfeld M, Kwak P, Vinokur M (1991) Unsteady incompressible Navier–Stokes equations. J Comput Phys 94:102–137
16. Saiki EM, Biringen S (1996) Numerical simulation of a cylinder in uniform flow: application of a virtual boundary method. J Comput Phys 123:450–465
17. Su SW, Lai MC, Lin CA (2007) An immersed boundary technique for simulating complex flows with rigid boundary. Comput Fluids 36:313–324
18. Tritton DJ (1959) Experiments on the flow past a circular cylinder at low Reynolds number. J Fluid Mech 6:547
19. Tseng YH, Ferziger JH (2003) A ghost-cell immersed boundary method for flow in complex geometry. J Comput Phys 192:593–623
20. Verzicco R, Yusof JM, Orlandi P, Haworth D (2000) Large eddy simulation in complex geometric configurations using boundary body forces. AIAA J 38((3):427–433
21. Williamson CHK (1996) Vortex dynamic in the cylinder wake. Annu Rev Fluid Mech 28:477
22. Ye T, Mittal R, Udaykumar HS, Shyy W (1993) An accurate Cartesian grid method for viscous incompressible flows with complex immersed boundaries. J Comput Phys 156:209–240
23. Yusof JM (1996) Interaction of massive particles with turbulence. PhD dissertation, Department of Mechanical and Aerospace Engineering, Cornell University
24. Yusof JM (1997) Combined immersed-boundary/B-spline methods for simulations of flow in complex geometries, Annual Research Briefs, Center for Turbulence Research, pp 317–327
25. Zhang N, Zheng ZC (2007) An improved direct-forcing immersed-boundary method for finite difference applications. J Comput Phys 221:250–268